CALPHAD-aided synthesis and characterization of an Al–Co–Cr–Fe–Ni–W high-entropy alloy prepared by arc melting and spark plasma sintering

L. Fenocchio, A. Saviot, S. Gambaro, Sophie Le Gallet, F. Valenza, Maria-Rosa Ardigo-Besnard, G. Cacciamani

Journal of Materials Research and Technology 34 (2025) 1252–1264

Contents lists available at ScienceDirect

Journal of Materials Research and Technology

journal homepage: www.elsevier.com/locate/jmrt

CALPHAD-aided synthesis and characterization of an Al–Co–Cr–Fe–Ni–W high-entropy alloy prepared by arc melting and spark plasma sintering

L. Fenocchio [a,1], A. Saviot [b,1], S. Gambaro [c], S. Le Gallet [b], F. Valenza [c], M.R. Ardigo-Besnard [b,*], G. Cacciamani [a,c]

[a] University of Genova, Chemistry and Industrial Chemistry Department (DCCI), Via Dodecaneso 31, 16146, Genova, Italy
[b] Laboratoire Interdisciplinaire Carnot de Bourgogne (ICB), UMR 6303 CNRS-Université de Bourgogne, 9 Av. Alain Savary, BP 47870, 21078, Dijon, France
[c] National Research Council (CNR), Institute of Condensed Matter Chemistry and Technologies for Energy (ICMATE), Genova, 16149, Italy

ARTICLE INFO

Handling Editor: P Rios

Keywords:
High-entropy alloys
Spark plasma sintering
Arc melting
CALPHAD modelling

ABSTRACT

In the present work, the novel $Al_{0.15}CoCrFeNiW_{0.15}$ High-Entropy Alloy (HEA) has been designed by CALPHAD (CALculation of PHAse Diagrams) computations with the in-house built Genova High-Entropy Alloys (GHEA) database, aiming to a mostly monophasic face-centered cubic (FCC) alloy strengthened by the precipitation of secondary μ phase. To explore different preparation routes, alloy samples have been synthesized by both arc melting (AM) and spark plasma sintering (SPS). Samples were characterized by low optical microscopy (LOM), scanning and transmission electron microscopy (SEM and TEM), X-ray diffraction (XRD), and microhardness measurements. Long-term annealing at 1100 °C has been performed, followed by quenching or furnace cooling. AM as-cast sample showed a monophasic FCC microstructure, characterized by large grains. Precipitation of μ phase was observed in the equilibrated and quenched sample, in good agreement with the thermodynamic calculations. On the other hand, SPS samples resulted in a finer microstructure, characterized by the presence of small particles of Al_2O_3 and μ phase, already present before annealing. Contrary to the thermodynamic predictions, after equilibration and quenching, the dissolution of the μ phase was observed due to the Gibbs-Thomson effect, which enhanced W solubility in the FCC solid solution. Annealing of the SPSed alloy followed by furnace cooling, however, allowed the precipitation of μ, thanks to the slower cooling rate. Overall, this study highlighted CALPHAD's utility for composition selection in complex multicomponent systems and demonstrated how AM and SPS lead to significantly different microstructures and properties, with grain size playing a key role in determining the alloy performances.

1. Introduction

High-Entropy alloys (HEAs) are a relatively new class of alloys developed over the past two decades, following pioneering research by Cantor and Yeh, which led to the discovery of the single-phase FCC CoCrFeMnNi composition, known as "Cantor alloy" [1,2]. This opened the way to the development of new multicomponent compositions exhibiting simple crystal structures, generally single-phase or biphasic [3,4]. One of the most studied HEA systems is the AlCoCrFeNi family, particularly thanks to the presence of Al that allows the transition from face-centered cubic (FCC) to body-centered cubic (BCC) single phase structures [5]. In order to improve mechanical properties, the solid solution strengthening effect by addition of alloying elements to the equimolar composition has been investigated, demonstrating that various elements, such as Ti, Nb, Zr or V have a strengthening effect by increasing the initial yield strength [6–9].

As for their preparation, HEAs are typically synthesized by arc melting (AM), which consists in a fast and reliable method to minimize sample manipulations and contaminations. However, powder metallurgy techniques offer interesting benefits, representing a valid alternative [10,11]. Spark plasma sintering (SPS) is one of the most used powder metallurgy processing routes, known for achieving significant densification rates by heating the powder via Joule effect. This process also allows to control the grain growth, thereby facilitating the achievement of fine microstructures. Two routes exist for the powder elaboration: gas atomization, which allows the direct production of HEA

* Corresponding author.
E-mail address: maria-rosa.ardigo-besnard@u-bourgogne.fr (M.R. Ardigo-Besnard).
[1] These authors contributed equally to the publication and have to be considered as joint first authors listed in alphabetical order.

https://doi.org/10.1016/j.jmrt.2024.12.140
Received 1 November 2024; Received in revised form 8 December 2024; Accepted 18 December 2024
Available online 19 December 2024

powders, and mechanical alloying, which consists in milling a mixture of elemental powders. In W-reinforced TiAl alloys, gas atomization was found to result in chemical heterogeneities (i.e., W segregation), reducing the mechanical properties [12]. In addition, it has been demonstrated that powder milling + SPS is effective for HEAs containing elements with very different melting points, such as Al and W [13].

Within this framework, thermodynamic calculations are an essential tool for screening wide compositional ranges to determine new compositions of interest. Investigations conducted in the last years by the Computational Thermodynamics of Materials (COMAT) research group at the University of Genova led to the development of the Genova High-Entropy Alloys (GHEA) thermodynamic database, which has been successfully applied to the study of phase relations [14,15] and graphite wettability [16] by Al–Co–Cr–Fe–Ni-R (R═Mo, Ta, W) HEAs. These works highlighted the robustness of the database by combining thermodynamic predictions with experimental validation. However, the investigated equiatomic compositions resulted in brittle alloys characterized by a biphasic BCC-B2 + intermetallic microstructure.

In the present study, a new HEA belonging to the Al–Co–Cr–Fe–Ni–W system was selected through thermodynamic calculations and experimentally investigated. Low Al content compositions, such as $Al_{0.3}$CoCrFeNi, have garnered significant interest due to their FCC structure that can be strengthened by various precipitates such as intragranular $L1_2$ or intergranular BCC-B2 phases [17–19]. The effect of W addition to the quinary system has not been widely investigated, especially at low Al-content. Available literature shows that, in the case of the near-eutectic composition $AlCoCrFeNi_2$, W addition results in increased mechanical resistance accompanied by decreased ductility [20]. On the other hand, according to our calculations, the FCC solid solution in the quinary system is widened by a decreasing Al content. Accordingly, a low-Al quinary HEA of $Al_{0.15}$CoCrFeNi composition was selected as starting alloy to simulate the effect of W addition by thermodynamic calculations. The target consisted in a W-containing FCC alloy, possibly solidifying as monophasic in the as-cast state, where the precipitation of a secondary phase could be tuned by performing an appropriate thermal treatment. Candidate compositions to be investigated experimentally were simulated with the aid of the thermodynamic calculations, and the final $Al_{0.15}CoCrFeNiW_{0.15}$ composition was selected, prepared and characterized. Additional details on the choice of the investigated composition are given in Section 2 of the present work.

The selected $Al_{0.15}CoCrFeNiW_{0.15}$ alloy has been prepared by both arc melting and powder milling + SPS to highlight and analyze the effect of the two preparation processes on the final state of the alloys. Thermodynamic calculations were used to design processing routes and support interpretation of the experimental results, which in turn were used to validate the thermodynamic database. Moreover, the microstructures and the phases resulting from the two manufacturing techniques were compared. Hardness measurements were performed to investigate the effect of the preparation method and of the thermal treatment. Finally, thermal stability of the microstructures and phase transformation occurring after long-term annealing were evaluated.

Summarizing, this study investigates the use of different synthesis techniques on the same Al–Co–Cr–Fe–Ni–W HEA composition, specifically designed by using the CALPHAD method. To the best of our knowledge, no prior studies in the literature have conducted such an analysis of the effects of the preparation method on the microstructure of a senary HEA. By comparing the two synthesis routes, this work demonstrates that spark-plasma sintering represents a viable alternative to arc melting, particularly in cases where the alloying elements pose challenges to conventional melting processes. By focusing on how synthesis routes influence critical parameters such as grain size, phase stability and microhardness, this work provides new insights into the relationship between preparation techniques and microstructural properties of HEAs.

2. Thermodynamic modelling

2.1. The GHEA thermodynamic database

The Al–Co–Cr–Fe–Ni–W thermodynamic database used in the present work is a subset of the wider GHEA database. In GHEA, all binary and ternary subsystems of the Al–Co–Cr–Fe–Ni–W senary system are modeled in their full temperature and composition ranges. Binary and ternary interaction parameters have been generally adapted from literature to ensure compatibility within GHEA phase models and lower-order parameters. Selected systems, however, have been completely assessed or re-assessed in view of GHEA [14,21–23]. The main features of the Al–Co–Cr–Fe–Ni–W database, such as phase models, assessment procedure, evaluation of metastable/unstable endmembers etc., have been presented in a previous paper [15]. For this reason, only a brief summary of the main phases appearing in the present investigation, together with their crystal structures and phase models is reported in Table 1.

2.2. Choice of the alloy composition

As mentioned in Section 1, Al_xCoCrFeNi HEAs with reduced Al content can exhibit interesting properties given by their mainly FCC microstructure strengthened by smaller amounts of BCC-B2 or $L1_2$ phases, depending on the composition. Al is known to be a strong BCC-B2 stabilizer, so that further reducing its content would lead the structure to be substantially monophasic FCC, possibly resulting in a ductile but low-hardness alloy. In Co-based superalloys, the mechanical properties are improved by secondary precipitation of hard phases such as carbides or intermetallics. According to thermodynamic calculations and experimental measurements in the literature, the amount of precipitated hardening phases is usually <5 mol %, to obtain significant hardening without excessive embrittlement [24,25]. Based on that, it would be interesting to search for a similar concentration of hardening phases in a mostly monophasic FCC HEA of the here investigated senary system. The reduction of the Al content, while promoting the formation of a wide FCC solid solution, might completely suppress the formation of BCC-B2, so that some other alternatives are needed to obtain precipitation hardening. The addition of a refractory metal might address this issue, favoring the formation of small amount of intermetallics. However, the alloying of additional elements in a solid solution usually decreases its melting point, so that in view of possible high-temperature applications, it is important to obtain the target strengthening while limiting the melting temperature decrease by accurate selection of quantity and quality of additives. Based on the mentioned constraints, the addition of W to the starting quinary system has been considered as a promising solution.

Within this framework, the GHEA thermodynamic database has been used as a fundamental tool to design the target composition, reducing

Table 1
Crystal structure and sublattice models of the main phases involved in the present work.

Phase	Pearson symbol - Prototype	Sublattice Model
FCC-A1 ([a])	*cF*4 – Cu	$(Al,Co,Cr,Fe,Ni,W)_1$ $(Va)_1$
FCC4 ($L1_2$ and $L1_0$)	*cP*4 – $AuCu_3$ *tP*4 – AuCu	$(Al,Co,Cr,Fe,Ni,W)_{0.25}$ $(Al,Co,Cr,Fe,Ni,W)_{0.25}$ $(Al,Co,Cr,Fe,Ni,W)_{0.25}$ $(Va)_1$
BCC-A2 ([b])	*cI*2 – W	$(Al,Co,Cr,Fe,Ni,W)_1$ $(Va)_3$
BCC-B2	*cP*2 – CsCl	$(Al,Co,Cr,Fe,Ni,W)_{0.5}$ $(Al,Co,Cr,Fe,Ni,W)_{0.5}$ $(Va)_3$
μ	*hR*36 – W_6Fe_7	$(Al,Co,W)_4$ $(Al,Co,Cr,Fe,Ni,W)_2$ $(Al,Co,Cr,Fe,Ni,W)_1$ $(Al,Co,Cr,Fe,Ni,W)_6$

[a] Disordered contribution to FCC4.
[b] Disordered contribution to BCC-B2.

the number of required experimental tests. The first step consisted in choosing a starting Al–Co–Cr–Fe–Ni composition. From the $Al_{0.3}$CoCrFeNi composition, already investigated in the literature [13,17–19], we tried further reducing the Al content to extend the FCC-A1 monophasic field down to lower temperatures. The vertical Al_xCoCrFeNi section calculated with GHEA is reported in Fig. 1a. Considering the uncertainties related to both experiments and calculations, n(Al) = 0.15 was chosen as a reasonable Al amount to ensure obtaining a monophasic quinary FCC alloy down to below 700 °C. The Equilibrium Phase Fraction (EPF) vs temperature plot for the chosen starting $Al_{0.15}$CoCrFeNi quinary composition is here reported in Fig. 1b.

Starting from this composition, the addition of W was simulated. The vertical $Al_{0.15}$CoCrFeNiW_x section is reported in Fig. 2a. Previous investigations on HEAs prepared by SPS [10,13], indicate that complete densification is obtained at about 1070–1080 °C, suggesting that the SPS cycle can be effectively performed at 1100 °C. According to the thermodynamic calculations, at this temperature we enter the two-phase field, FCC-A1 + μ, when n(W) ~ 0.15 (Fig. 2b). Bae et al. [26] demonstrated that, in non-equiatomic CoCrFeNiMo_x HEAs, the dispersion of μ phase in a FCC matrix is a promising route to improve mechanical properties. By simulating further cooling of the chosen composition (EPF vs T plot in Fig. 2c), we found that the amount of secondary μ phase between complete densification temperature and sintering temperature remains within the target <5 mol % range. Considering the uncertainties related to experimental alloy preparation and characterization, determination of the densification temperature, and thermodynamic calculations, this amount of secondary phase was considered satisfactory to obtain hardening without excessive alloy embrittlement.

3. Materials and methods

Two $Al_{0.15}$CoCrFeNi$W_{0.15}$ HEAs were synthesized by using two different preparation methods: AM and SPS. Samples were then annealed at 1100 °C for 14 d and water-quenched or furnace cooled. Details on the sample preparation procedures are reported in Section 3.1 and summarized in Table 2.

3.1. Sample preparation

3.1.1. Preparation by AM

The $Al_{0.15}$CoCrFeNi$W_{0.15}$ alloy of about 1 g was prepared by arc melting the appropriate quantities of the pure metals (purity >99.9 %) under Ar atmosphere and using a Zr getter. Considering that the melting point of W exceeds the boiling point of Al, possibly resulting in Al depletion or presence of unreacted W in the final alloy, preliminary binary Ni–W alloys were first arc melted and subsequently combined with the remaining elements to obtain the target senary alloy. To ensure compositional homogeneity, the alloys were flipped and re-melted up to five times. The so-prepared alloy was then cut in two parts: one was analyzed as synthesized (AM_AS sample), and the other (AM_1100 sample) was annealed at 1100 °C for 14 d (see Section 3.1.3 for details on the annealing procedure).

3.1.2. Preparation by SPS

For the preparation of the $Al_{0.15}$CoCrFeNi$W_{0.15}$ alloy by SPS (SPS_AS sample), high-purity elemental powders (>99.2 %) of Al, Co, Cr, Fe, Ni, and W were subjected to planetary ball milling (Fritsch Pulverisette 4) to chemically homogenize the mixture. The initial particle sizes are detailed in Table 3.

Stainless hardened steel milling bowls (250 mL) and balls (10 mm diameter) were used for the milling, and the mass ratio between balls and powders (BPR) has been set to 7:1. The rotation speed of the central disk and grinding jars were respectively set to 250 and − 250 rpm, and the milling cycle consisted of 1 h of milling followed by pauses of 30 min repeated 16 or 28 times. No process control agent (PCA) was used during ball milling to prevent carburization of the alloys. The milling jars were prepared under Ar atmosphere to limit oxygen contamination. SPS (FCT Systeme GmbH HPD 10) has been performed in a graphite die with internal diameter of 30 mm. Sintering parameters were set to 1100 °C, reached with a heating rate of 50 °C/min, and a pressure of 80 MPa applied during the whole cycle. A dwell time of 30 s was applied, followed by free cooling to room temperature. As for powder mechanical activation, the sintering matrix was prepared under Ar atmosphere, and the SPS cycle was performed under vacuum, to limit any oxygen contamination.

3.1.3. Annealed samples

Both the AM and the SPS samples were annealed to ensure equilibration at the same temperature of 1100 °C (AM_1100 and SPS_1100 samples, respectively) to better compare the effects of the two different preparation routes. In both cases, samples were wrapped in Ta foils, enclosed in quartz vials under inert atmosphere, heat treated for 14 d at 1100 °C in an electric furnace and then water quenched. The annealing temperature of 1100 °C, equal to the sintering temperature, was chosen

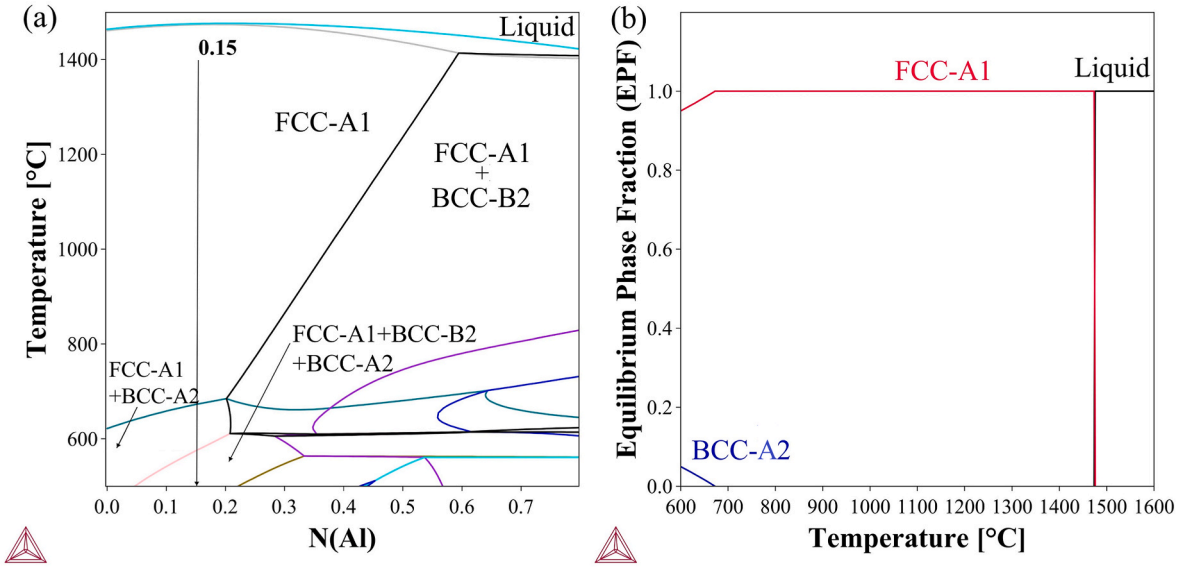

Fig. 1. (a) Vertical Al_xCoCrFeNi section and (b) Equilibrium Phase Fraction (EPF) vs temperature plot for the $Al_{0.15}$CoCrFeNi composition.

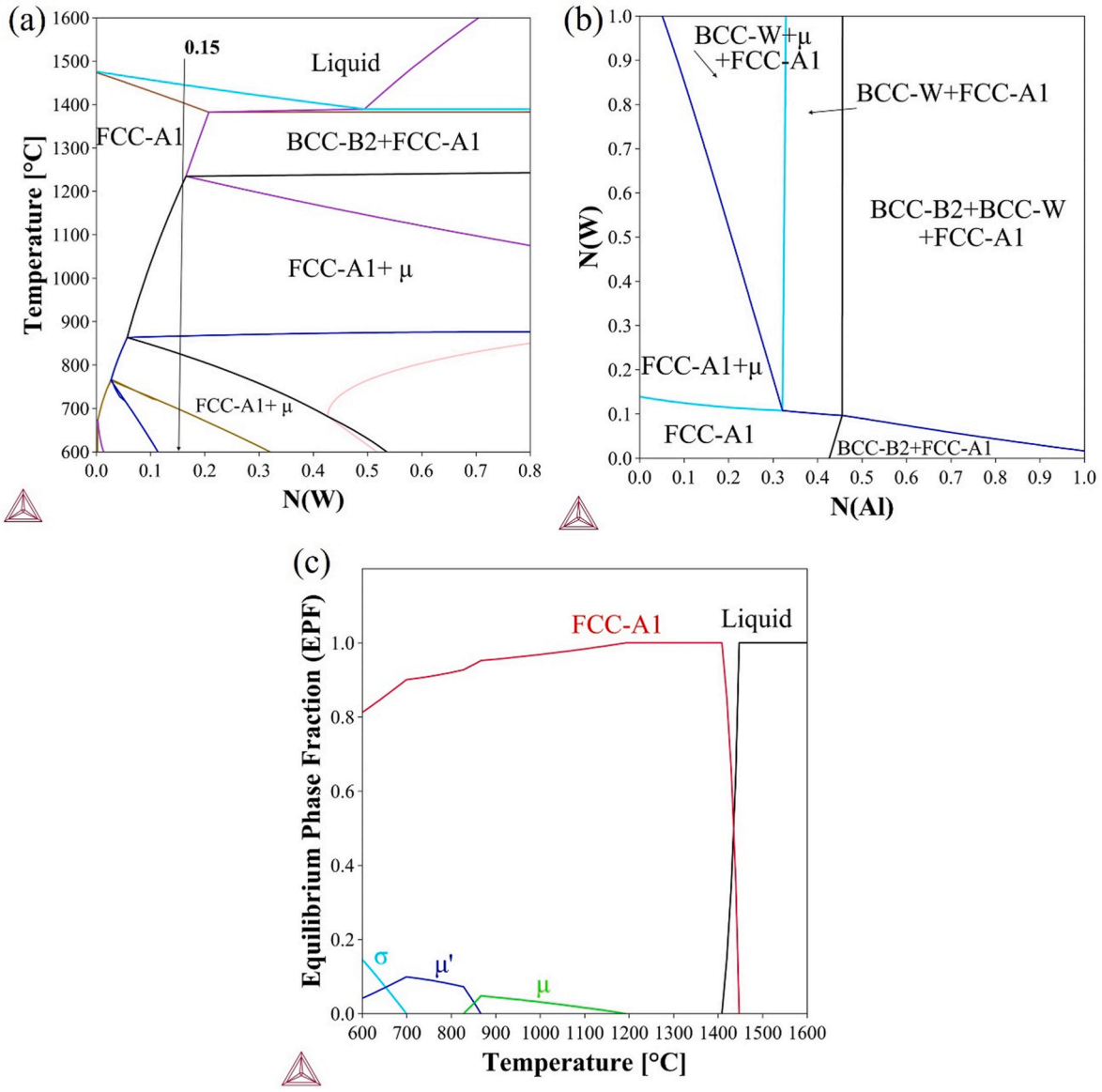

Fig. 2. (a) Vertical $Al_{0.15}CoCrFeNiW_x$ section; (b) $Al_xCoCrFeNiW_y$ isothermal section at 1100 °C and (c) Equilibrium Phase Fraction (EPF) vs temperature plot for the $Al_{0.15}CoCrFeNiW_{0.15}$ composition.

Table 2
List of the prepared samples with the related name, synthesis procedure, and thermal treatment.

Synthesis	Thermal Treatment	Sample name
Arc melting (AM)	As-cast	AM_AS
	Annealed 14d at 1100 °C and quenched	AM_1100
Spark plasma sintering (SPS)	As sintered	SPS_AS
	Annealed 14d at 1100 °C and quenched	SPS_1100
	Annealed 14d at 1100 °C and furnace cooled	SPS_1100_FC

Table 3
Particle sizes of the commercial powders (Alfa Aesar, Neyco*).

Element	Al	Co	Cr	Fe	Ni	W*
Powder particle size (μm)	44	1.6	<10	<10	3–7	<10

aiming to verify microstructural differences between sintering and equilibration at the same temperature. An additional alloy prepared by SPS was subjected to annealing at 1100 °C followed by furnace cooling (SPS_1100_FC sample), aiming to allow precipitation and growth of μ phase crystals; additional details are presented in Section 4.2.2.

3.2. Samples characterization

3.2.1. Sample prepared by AM (AM_AS and AM_1100)

The AM prepared samples were cross-sectioned and then mechanically polished with diamond paste down to 1 μm grit. The microstructure was analyzed by scanning electron microscopy (SEM – model: LEO 1450 VP) coupled with energy-dispersive X-ray spectroscopy (EDS – Oxford Instruments, 7353 model with Oxford-INCA software v.4.07). Additionally, chemical etching (for 20 s in aqua regia, in agreement with [27]) and Light Optical Microscopy (LOM – Model: LEICA DM 4000 M) were used to highlight grain boundaries. X-Ray Diffraction (XRD) analysis was performed with a powder diffractometer (Siemens D-500) using the *Cu* K_α radiation. XRD was carried out on the polished surface of bulk samples. The hardness of the different samples was measured by

using a Vickers indenter (Leica VM HT MOT), with a load of 500 g. At least 5 indentations were performed for each measurement, provided that the distance between indentations was higher than three times the length of their diagonal. Large indentations were performed encompassing the different phases in the samples to evaluate the overall alloy hardness, given the impossibility to isolate the single contributions of the smaller crystals.

3.2.2. Sample prepared by SPS (SPS_AS, SPS_1100, SPS_1100_FC)

The surfaces of the SPS prepared samples were mechanically polished similarly to those of the AM samples. In addition, a super finishing step was performed using a colloidal silica suspension of 0.03 μm.

Sample surfaces were analyzed by XRD with *Cu* K_α radiation (Bruker D8 Discover). Microstructural characterizations of the samples before and after annealing treatment were performed by SEM-EDS (model: JEOL JSM 7600F). In the case of the SPS_AS sample, transmission electron microscopy (TEM) analyses were also carried out. A thin lamella was taken from the sample by focused ion beam (FIB), using a dual beam FIB/SEM ThermoFisher Helios NanoLab600i apparatus. The extracted lamella (10 × 5 μm) was then thinned to a thickness of around 50 nm using the focused Ga ion beam, accelerated to 5 kV for the final step to limit irradiation defects. TEM- and scanning transmission electron microscopy (STEM)-EDS characterizations were performed with a JEOL JEM-2100F apparatus, operating at an accelerating voltage of 20 kV. Vickers hardness measurements were performed using a ZHμ HD (Zwick Roell) indenter with a load of 500 g.

4. Results and discussion

The EDS-measured global compositions of the samples are reported and compared to the target nominal composition in Table 4. Results on AM and SPS samples are reported in Sections 4.1 and 4.2, respectively. Finally, in Section 4.3, results are globally analyzed and critically discussed, comparing the two different synthesis routes.

4.1. Samples prepared by AM

4.1.1. As-cast sample (AM_AS)

The overall composition of the AM_AS sample is close to the nominal one (Table 4), suggesting that the synthesis route has been effective. The microstructure of the AM_AS sample is reported in Fig. 3a, resulting homogeneous and substantially monophasic. The SEM micrograph shows a certain shading, which however does not correspond to significant compositional difference between darker and lighter areas, as also confirmed by EDS maps (see supplementary material S1). The sample was then chemically etched in aqua regia (20 s), aiming to reveal the grain boundaries in the LOM image (Fig. 3b).

However, based on previous experiences on alloys of this kind ([28] and other unpublished results, see supplementary material S2) presenting grain size in the order of some tens of microns, and giving the dimensions of the areas having different grey contrast visible in Fig. 3b, these latter possibly correspond to domains of grains similarly oriented, rather than to the single grain edges. This is also due to the high homogeneity of this monophasic sample, which makes it difficult to reveal individual grain boundaries through chemical etching. Several other chemical etchants were attempted, based on previous experiences (e.g. 5 g $FeCl_3$ + 25 mL HCl +5 mL HNO_3 + 25 mL H_2O, like in supplementary material S2) or literature investigations (e.g. 5 g Cu_2SO_4 + 25 mL Ethanol +25 mL HCl, like in Ref. [29]), but none of them turned out to be effective.

The XRD analysis has been performed on the polished bulk sample in the 30–90° 2θ range, confirming its substantial monophasicity. Only one peak of scarce intensity at $2\theta = 81°$ could not be properly indexed. It possibly belongs to some residual Cr, which has entered the FCC solid solution or formed μ phase during the annealing, as the peak substantially disappears in the XRD pattern of the AM_1100 sample (Fig. 4). As for the hardness measurements, an overall value of 382 ± 5 $HV_{0.5}$ was obtained for the AM_AS sample.

Table 4
Comparison between nominal and experimental compositions (measured by EDS) of the prepared samples.

Composition (mol %)	Al	Co	Cr	Fe	Ni	W
Nominal	3.5	23.5	23.5	23.5	23.5	3.5
AM_AS	3.2	24.0	23.3	23.3	23.0	3.2
AM_1100	3.5	23.3	23.3	23.4	23.0	3.5
SPS_AS	3.9	23.2	23.3	23.0	22.6	4.0
SPS_1100	4.1	23.3	22.7	23.5	23.1	3.6
SPS_1100_FC	4.0	22.8	23.1	23.1	23.1	3.9

4.1.2. Sample annealed at 1100 °C (AM_1100)

The LOM image of the AM_1100 sample after chemical etching is reported in Fig. 5a. In this case, aqua regia was effective in highlighting the grain boundaries, so that equiaxed grains with an average size of 60 μm and several lamella-shaped annealing twins can be distinguished. This is also confirmed by the SEM image in SE mode reported in Fig. 5b. The SEM image in BSE mode (Fig. 5c) was acquired before etching and shows a biphasic microstructure with one main dark-grey phase surrounding smaller crystals of a bright W-rich phase. The main phase corresponds to the FCC solid solution, while the secondary brighter phase corresponds to the μ intermetallic precipitating at the grain boundary, as also underlined by the etching. The composition of the two phases measured by EDS is reported and compared with calculations in Table 5. It is noteworthy that all the Al present in the alloy remains in the solid solution, since its solubility in the μ phase is extremely limited. Element distribution between the FCC matrix and the μ intermetallic was evaluated by EDS mapping, reported in Fig. 5e on area of Fig. 5d.

The phase analysis resulting from SEM-EDS was compared to the phase amounts and compositions calculated using the CALPHAD (CALculation of PHAse Diagrams) approach (Table 5). Phase amounts in mole fraction (of atoms) were qualitatively evaluated assuming their equivalence to the surface fractions determined by image analysis (software GIMP). Such an approximation is justified by the small variation between the molar volumes of metals and alloys. The so-estimated experimental phase amounts are in good agreement with those predicted by calculations, especially considering the uncertainty related to the surface defects (e.g. holes) in the samples. As for phase compositions, very good agreement between calculations and EDS measurements can be observed for FCC. For the μ phase, the main compositional features (absence of Al and concentration of W higher than all other elements) are correctly reproduced by the calculations, but Co and Cr concentrations are respectively over- and under-estimated. As for Fe, the difference between calculated and experimental content lies within a satisfactory range of agreement.

The XRD analysis (green pattern in Fig. 4) confirmed the presence of the FCC solid solution. The additional peaks detected in the AM_AS sample substantially disappear in this pattern, suggesting that the annealing treatment was successful in eliminating the possibly related traces of unreacted Cr. As for the secondary W-rich bright phase appearing in the micrograph, its composition is similar to that of the μ phase revealed by TEM-EDS analyses performed on the SPS_AS sample (see Section 4.2.2). By analogy, and with the support of the thermodynamic calculations, this W-rich phase is further confirmed to correspond to μ. As for the hardness measurements, an overall value of 233 ± 16 $HV_{0.5}$ was obtained for the AM_1100 sample. With respect to the as-cast sample, the hardness is significantly decreased, probably due to the relaxation of the microstrains related to the as-cast state, and to the grain growth related to the annealing. In this case, it is likely that such effects overcome the hardness increase expected from the μ phase precipitation, also due to its small quantity.

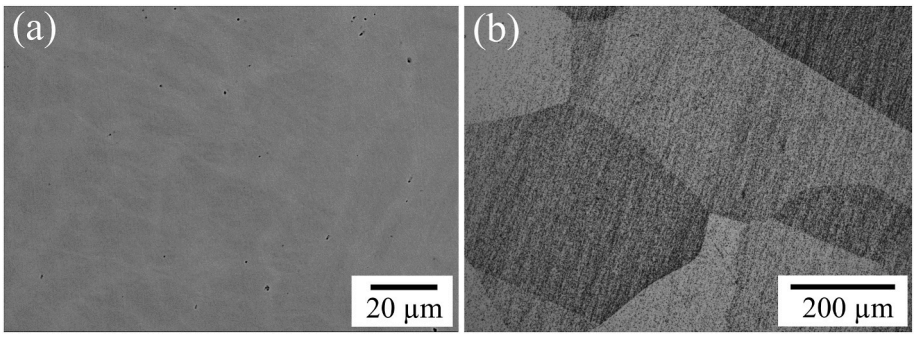

Fig. 3. (a) SEM backscattered electron image *of the AM_AS and (b) LOM image of the AM_AS sample after chemical etching.*

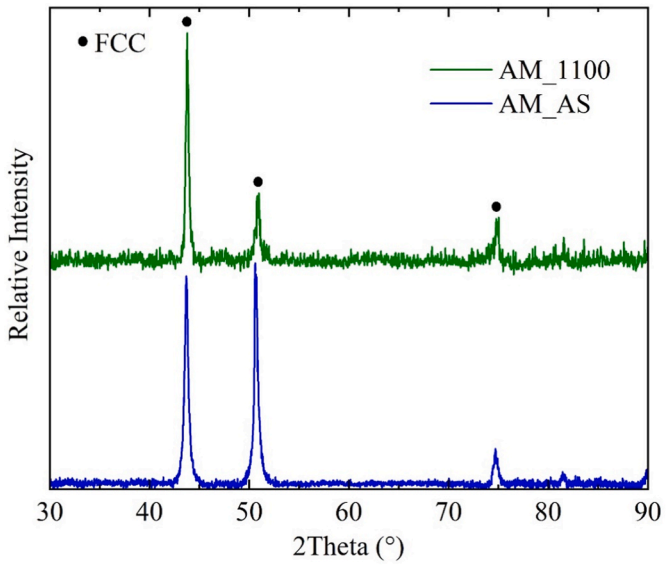

Fig. 4. XRD pattern for the AM_AS and AM_1100 samples.

4.2. Samples prepared by SPS

4.2.1. As-sintered sample (SPS_AS)

The SEM micrographs and XRD patterns of the powders after 16 and 28 h of ball milling are reported in Fig. 6. After 16 h of ball milling, an increase in particle size from an average of 13 (not-milled powder) to 200 µm was observed. This shorter mechanical activation led to the disappearance of Al and Co peaks, while slight traces of pure Cr were still detected and can be seen on the surface of the milled powders (green arrows in Fig. 6b). The characteristic peaks of pure W are also still visible, since small white W particles were observed on the powder surface (yellow arrows in Fig. 6b). All the peaks are broadened, possibly due to an increase of the microstrains and a decrease of the crystallite size. The asymmetry of the (200) peak at 51.4° with a broadening to lower angles indicates that the formation of the FCC solid solution has started.

Compared to 16 h of milling, increasing the milling time to 28 h leads to a reduction in particle size to an average of 80 µm (Fig. 6c). The XRD pattern of the 28 h milled powder (Fig. 6e) shows a shift of the (111) peak from 44.4 to 43.9°, indicating that the formation of the FCC solid solution by mechanical alloying is more advanced. However, the pure W characteristic peaks are still visible, highlighting its difficult diffusion into the solid solution during milling at low temperature. On the contrary, peaks related to pure Cr have almost completely disappeared. As planetary ball milling generally results in slight oxygen contamination, particularly in the case of very reactive powders such as the milled HEA composition tested in the present study, no longer milling times were investigated. Finally, the 28 h milled powder has been selected for sintering due to its higher chemical homogenization.

The XRD analysis of the SPS_AS sample reveals an FCC structure (Fig. 7), with no traces of pure W. Thermodynamic calculations at the sintering temperature (1100 °C) predict approximately 98.4 mol % FCC phase and 1.6 mol % W-rich µ phase. As in the case of the AM samples, the µ phase could not be detected in the XRD pattern, probably due to its low amount.

The global composition of the SPS_AS sample measured by EDS is close to the nominal one (Table 3), suggesting the effectiveness of the synthesis. The microstructure at low magnification (Fig. 8a) shows a heterogeneous distribution of white nanometric precipitates, mainly concentrated at the grain boundaries. In addition, a few large precipitates ~5 µm in size can be detected. The finer precipitates tend to be more concentrated in the areas closer to the larger ones rather than far from them. The FCC matrix is composed of a bimodal grain structure: the majority of the grains measure ~400 nm, and domains of ~10 µm are formed by micrometric grains, reaching 2 µm in size. Grains similar to the larger ones have already been observed in a previous study on the sintering of $Al_xCoCrFeNi$ alloys and are associated with dynamic recrystallization and abnormal grain growth at prior particle boundaries [13]. This phenomenon arises from the large number of crystalline defects generated by the milling stage. Fig. 8 also shows many dark nanometric precipitates, located at the grain boundaries across the entire surface of the sample. However, their small dimensions do not allow a precise determination of their composition by SEM-EDS. The Z-contrast in the BSE images indicates that the white precipitates may correspond to W-rich phases, such as the expected µ phase, or to some residual pure W. On the contrary, the darker precipitates are expected to contain lighter elements. In order to identify the nature of the nanometric dark and white precipitates, not detected by XRD and impossible to be certainly identified by SEM-EDS, TEM-EDS analysis has been performed.

STEM-EDS mapping displayed in Fig. 9 revealed that all the black precipitates are smaller than 50 nm and are Al- and O-rich. The measured composition (Point A in Table 6) indicates that they correspond to Al_2O_3 grains. Their relatively important presence can be attributed to the impurity of the starting elemental powders, combined with the inevitable oxygen contamination due to the milling stage. Slight compositional variations are also observed for the FCC phase, but its overall composition is in accordance with thermodynamic calculations and underlines that W has diffused in the FCC solid solution. Fig. 9 shows that all the white precipitates are characterized by significant W enrichment. When comparing the EDS measurements, micro and nanometric precipitates (points B and C in Table 6, respectively) exhibit almost the same composition. Some differences in Cr and Co contents in the µ phase with respect to the thermodynamic calculations can be observed, similarly to the AM samples, and are further commented in Section 4.3. However, based on these results, TEM-EDS analyses clearly demonstrate that the white precipitates do not correspond to residual W from the starting powder, but to the µ phase formed during sintering, in

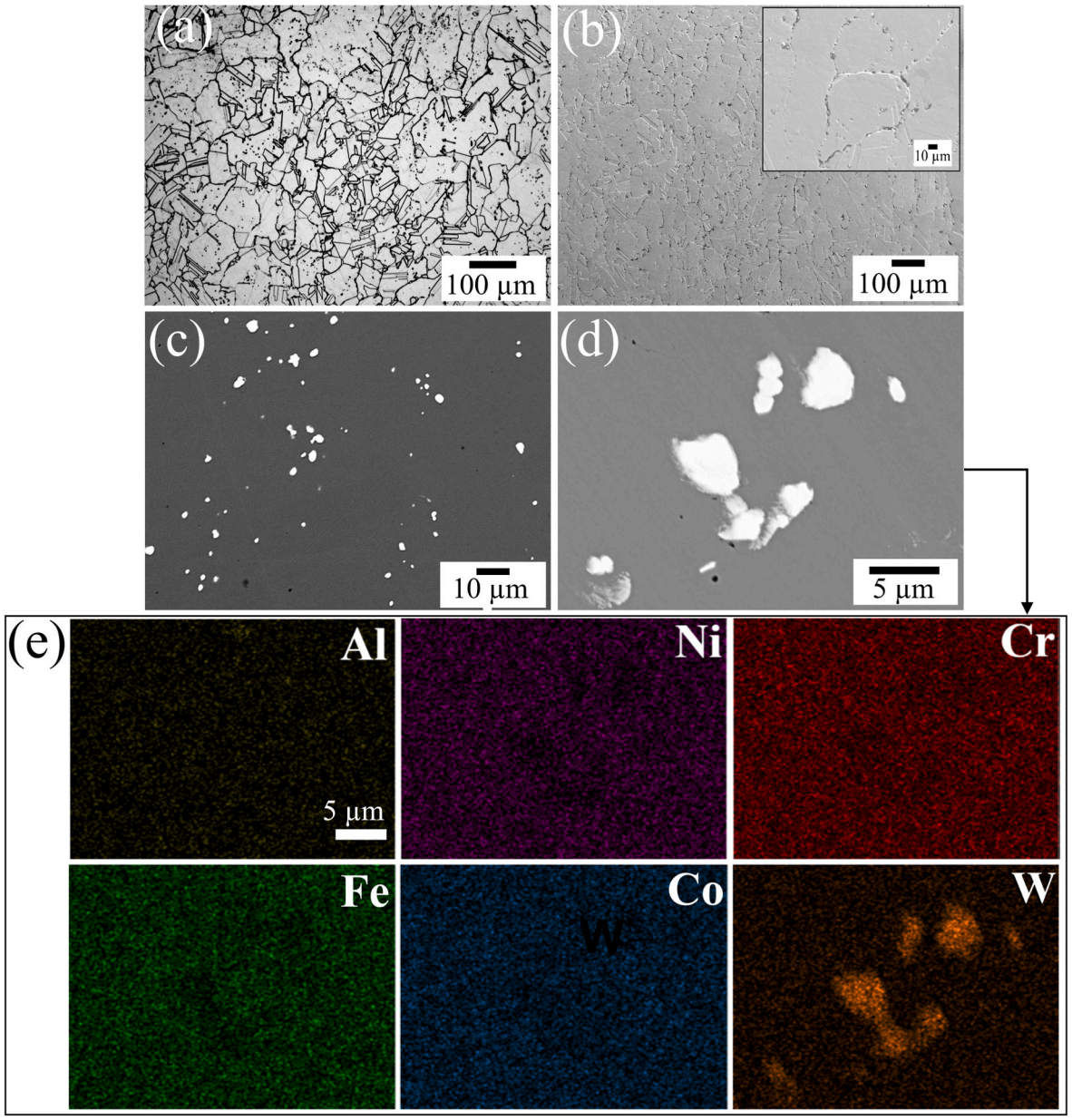

Fig. 5. AM_1100 sample: (a) LOM and (b) SEM (in secondary electron mode) images after chemical etching; (c) SEM image (in backscattered electron *mode); (d) detail at higher magnification and (e) related elemental EDS mapping.*

Table 5
Comparison between experimental and calculated equilibrium phase fractions (EPF, mol%) and compositions (mol %) of the phases detected in the AM_1100 sample.

Phase		EPF	Al	Co	Cr	Fe	Ni	W
FCC-A1	EXP	98.8	3.1	23.5	22.9	23.5	23.5	3.5
	CALC	98.4	3.5	23.2	23.5	23.5	23.5	2.8
μ	EXP	1.2	–	18.8	20.1	15.7	9.0	36.4
	CALC	1.6	–	24.9	8.0	11.2	9.8	46.1

agreement with thermodynamic predictions. Additionally, this underlines the success of the performed synthesis procedure by SPS.

The TEM image in Fig. 12 also suggests that the largest μ phase precipitates (Fig. 10a) are polycrystalline compared to the finest ones (Fig. 10c). In both cases, nano and micrometric μ phase grains present the same microstructure, characterized by a significant number of annealing twins (Fig. 10). The mechanical activation related to the milling procedure leads to an increase in crystal defects such as dislocations, whose high density may lead to the increase of active sites for twin nucleation [30]. Twinning is then promoted during the recrystallization that begins during the subsequent sintering process. A similar behavior was observed in previous works on a WMoFeNi HEA by Liu et al. [31,32], who highlighted the tendency of the μ phase to develop twin substructures with a high density of $(0001)_{\mu}$ nano-twins. In addition, SPS generally produces non-equilibrium microstructures, especially when combined with powder mechanical activation [33,34]. Moreover, in the present SPS sample the μ phase nanometric precipitates are more numerous and larger around the micrometric ones rather than far from them. Therefore, it is possible to attribute the formation of the μ phase to the heterogeneous distribution of W in the powder after milling, combined with the short dwell at high temperature during SPS, rather than to its thermodynamic stability at the sintering temperature of 1100 °C.

Microhardness measurements have been performed on the SPS_AS

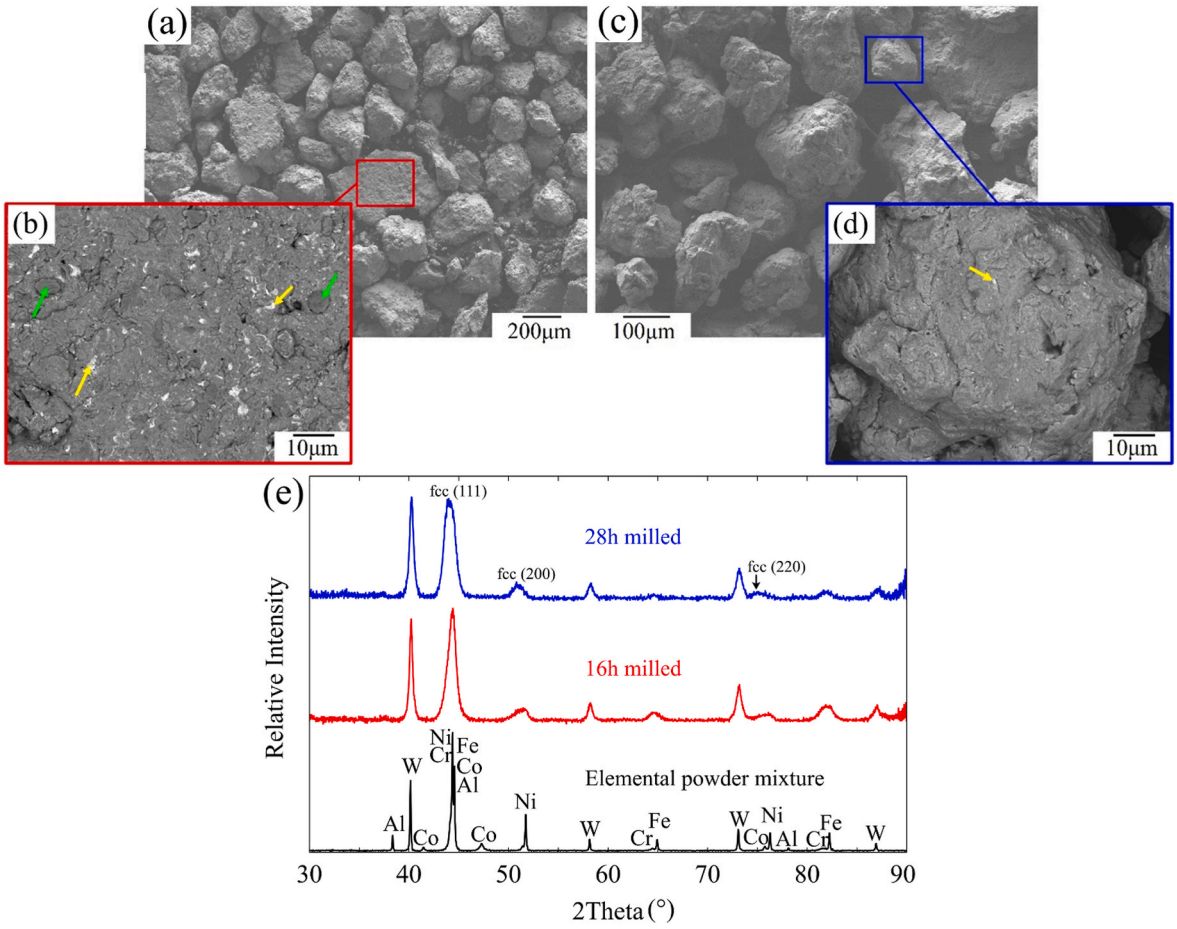

Fig. 6. SEM image of powder particles after a-b) 16 h and c-d) 28 h ball milling. Green and yellow arrows indicate pure Cr and W particles, respectively; e) XRD patterns of Al–Co–Cr–Fe–Ni–W elemental powder mixture as prepared and after 16 h and 28 h ball milling.

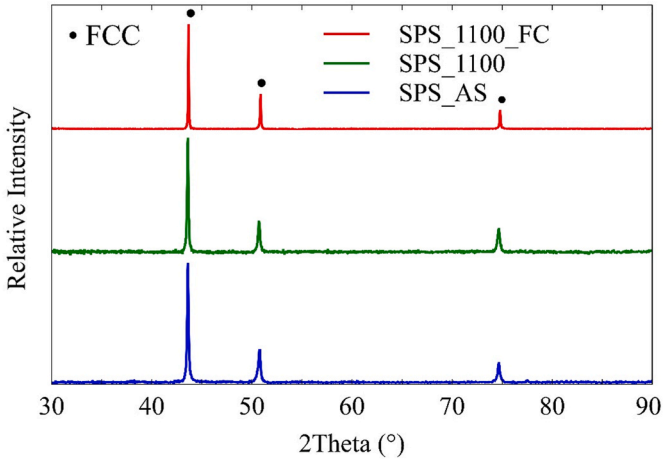

Fig. 7. XRD patterns of the SPS_AS, SPS_1100, and SPS_1100_FC samples.

sample. The hardness of 600 ± 15 $HV_{0.5}$ could be explained by the combined effects of the fine FCC grains of 400 nm, the presence of W in the solid solution and the numerous dispersed nanometric grains of Al_2O_3 and μ. For comparison, the $Al_{0.3}$CoCrFeNi HEA obtained by mechanical alloying and subsequent SPS, characterized by an FCC solid solution of similar grain size containing Cr carbide precipitates, has a hardness of 486 $HV_{0.5}$ [35]. Therefore, the important hardness increase observed in the present study seems to come from the fine distribution of μ phase precipitates at grain boundaries. Overall, the microstructure of the SPS_AS sample suggests a very brittle behavior.

4.2.2. *Sample annealed at 1100 °C (SPS_1100 and SPS_1100_FC)*

The XRD analysis (Fig. 7) indicates that after annealing followed by quenching, the SPS sample is still composed of an FCC structure. In the post-annealing microstructure of Fig. 11, the nanometric and micrometric grains of μ phase have been dissolved. This led to the diffusion and homogeneous distribution of all W into the FCC solid solution, as confirmed by the EDS mapping in Fig. 12. The elemental maps show that also Ni, Cr, Fe and Co are homogeneously distributed into the FCC matrix. The long-term annealing led to a growth of the FCC grains from around 400 to 800 nm. The black precipitates, which were already detected in the as sintered sample before annealing, still correspond to Al_2O_3. Their size increased during annealing, growing from about 18 to 300 nm. This result is in accordance with the works by Ida et al. [36,37], who highlighted the stability of Al_2O_3 precipitates in a NiCr nanostructured alloy, and observed a growth of the same order of magnitude after 100 h of annealing at 1100 °C.

The annealed sample shows a significant decrease in hardness to 300 ± 1 $HV_{0.5}$, which can be attributed to the dissolution of the μ phase and to the small grain growth. Contrary to the thermodynamic calculations, the μ phase was not observed in the annealed and quenched sample. At this point in the study, it is possible to suggest that this difference could be due to the grain size or the presence of Al_2O_3 at the grain boundaries, which may block μ phase nucleation and subsequent precipitation. Indeed, it is reported in the literature that the grain size can affect the thermal stability range of phases by Gibbs-Thompson effect [38,39].

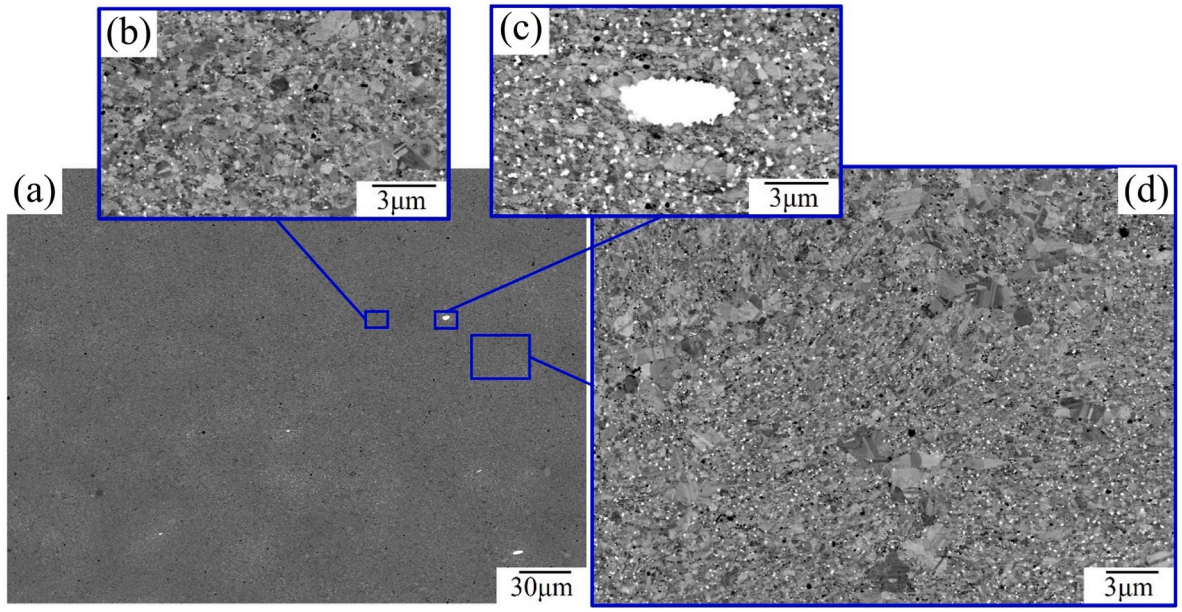

Fig. 8. a) SEM backscattered electron images of the SPS_AS sample, b) and d) magnified regions and c) magnified microstructure near a micrometric W-rich particle.

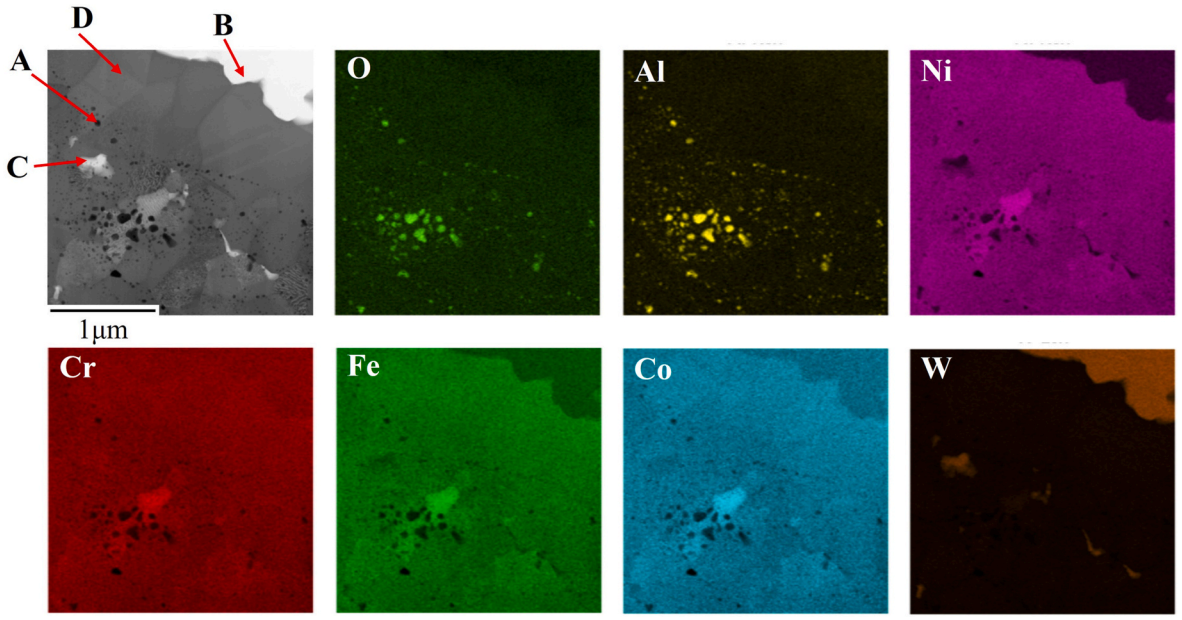

Fig. 9. STEM picture and EDS elemental mapping of the SPS_AS sample.

Table 6
Composition (at. %) of the different precipitates in the SPS_AS sample measured by EDS.

Point	O	Al	Co	Cr	Fe	Ni	W
A	61.6	37.7	0.2	0.2	0.2	0.1	0.0
B	1.4	0.4	18.6	23.4	15.5	5.2	35.5
C	1.3	0.4	17.8	20.1	14.5	5.5	40.4
μ (CALC)	/	–	24.9	8.0	11.2	9.8	46.1
D	2.2	2.3	23.9	23.6	24.1	21.2	2.7
FCC (CALC)	/	3.5	23.2	23.5	23.5	23.5	2.8

This effect results in enhanced W solubility in the FCC solid solution at 1100 °C, thereby favoring the dissolution of the small μ phase precipitates. In order, to verify this hypothesis, a new long-term annealing at 1100 °C has been performed on an as-SPS sample, followed by a furnace cooling. The microstructure of this SPS_1100_FC sample presents grains of about 1 μm in size, and Al_2O_3 is found mainly concentrated at grain boundaries. XRD analysis (Fig. 7), only revealed the presence of the FCC solid solution. Even if it was not detected by XRD, the μ phase was observed in the SEM micrograph as precipitates at grain boundaries (white crystals in Fig. 12). This confirms that μ phase precipitation in $Al_{0.15}CoCrFeNiW_{0.15}$ is not blocked by the presence of Al_2O_3 at the grain boundaries and occurs during cooling thanks to the very slow cooling rate. This observation suggests that for the SPS_1100 sample, the effect of grain size is to extend the stability of the FCC solid solution containing ~3.5 at. % of W down to lower temperatures, preventing μ phase precipitation at 1100 °C.

The hardness of the SPS_1100_FC sample reaches 330 ± 3 $HV_{0.5}$, indicating an increase of 30 HV compared to the SPS_1100 sample, most

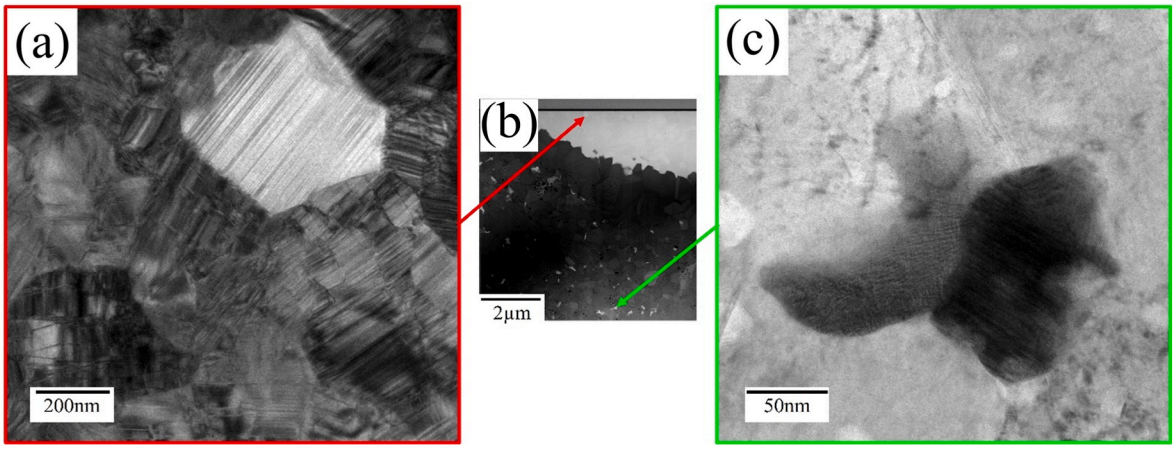

Fig. 10. TEM images of the SPS sample showing twin substructures inside a) micrometric and c) nanometric μ phase particle; b) shows the respective sample area.

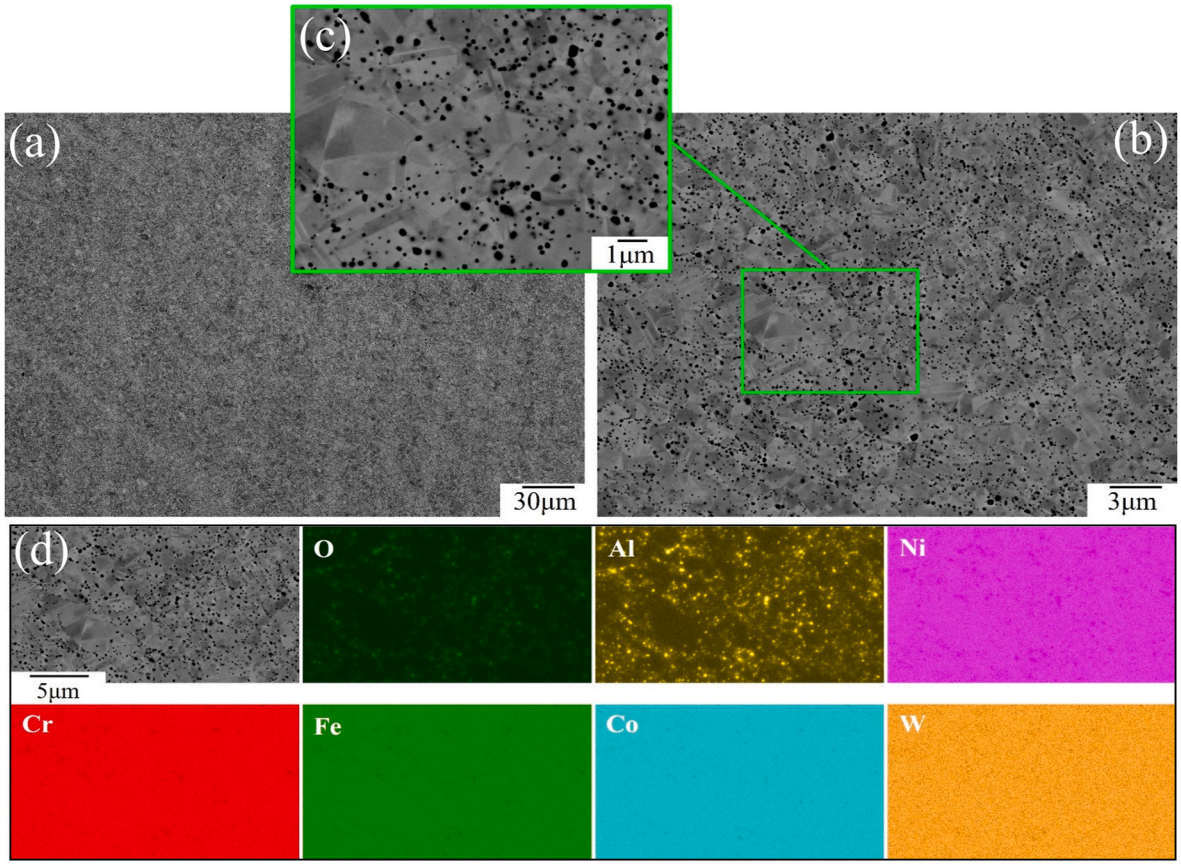

Fig. 11. a-c) SEM images in backscattered electron mode at different magnifications and d) EDS elemental mapping of the SPS_1100 sample.

likely due to the presence of the μ phase. As a reminder, the hardness of the SPS_AS sample, which also contains μ phase precipitates, is 600 $HV_{0.5}$. Image analyses, performed with GIMP software, revealed a surface fraction of μ phase in the SPS_1100_FC sample of about 1.2 mol%. This value is very close to that found for the SPS_AS sample, which is about 1.0 mol%. In both cases, the μ phase is mainly located at grain boundaries. However, in the SPS_AS sample, the μ phase precipitates are overall smaller (300 nm on average vs 600 nm on average for the SPS_1100_FC sample). Moreover, they present a finer distribution, except for some bigger micrometric precipitates randomly dispersed on the surface. The thinner grains, which enhance hardness by Hall-Petch effect, combined with a finer and homogeneous distribution of the μ phase precipitates, explain the hardness increase observed for the SPS_1100_FC sample. Finally, it is possible to underline that Al_2O_3 is substantially inert towards the metal HEA matrix, since no chemical interaction was observed in the samples, regardless of the treatment.

4.3. Comparison between AM and SPS samples

As expected, the present study underlines that the preparation method has an important influence on the final alloy microstructure. AM results in the formation of large FCC grains, whose chemical homogeneity is enhanced by the several re-meltings. In comparison, powder mechanical activation followed by SPS produces a nanostructured FCC

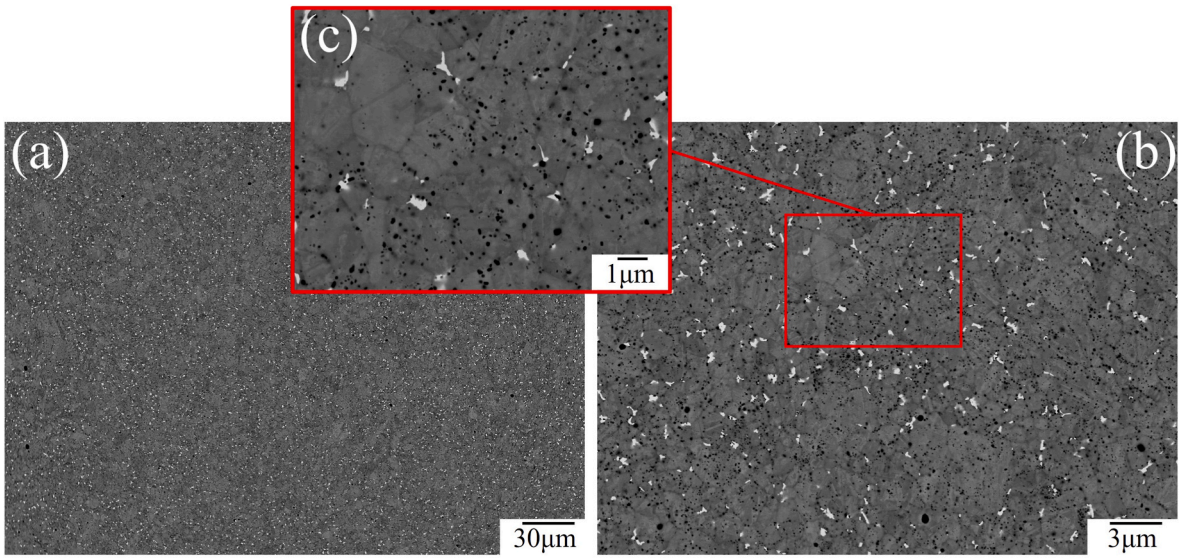

Fig. 12. SEM images in backscattered electron mode of the SPS_1100_FC sample at different magnifications.

matrix in which nanometric μ phase and alumina precipitates are dispersed. The heterogeneous distribution of W in the powder after milling, combined with the short dwell time at high temperature during SPS that limits elemental diffusion (especially for W), enhances the formation of μ phase crystals of reduced dimensions and non-homogeneously distributed. The thermodynamic calculations indicate the presence of both FCC and μ phase at 1100 °C, which is consistent with the results obtained from the SPS_AS and the AM_1100 samples. After long-term annealing at 1100 °C followed by quenching, the AM_1100 and SPS_1100 samples still exhibit very different behavior. In the case of the AM_1100 sample, the μ phase precipitation occurs at grain boundaries, whereas the μ phase formed during the sintering is dissolved in the case of the SPS_1100 sample, most likely due to the Gibbs-Thomson effect. This phenomenon enhances W solubility in the FCC solid solution at 1100 °C, thereby favoring μ phase dissolution. After annealing, the AM_1100 sample is consistent with thermodynamic predictions, whereas the SPS_1100 sample is not. The compositions of the μ phase (when present) formed using the different synthesis processes are very close (Table 7). In comparison with the CALPHAD predictions, a few differences exist, especially for the Co and Cr content, respectively over- and under-estimated with respect to the experimental measurements, regardless of the preparation method.

These discrepancies are probably attributable to the combination of a) the difficult evaluation of the numerous endmembers deriving from the 4-sublattice CALPHAD modelling of the μ phase (see Table 1), and b) the experimental uncertainties related to EDS measurements on crystals of such small dimensions. This might indicate that the stabilities of Co- and Cr-rich endmembers of the μ phase are respectively over- and under-estimated (or both). In principle, based on the present experimental information, they could be adjusted: however, modifying thermodynamic parameters relevant to more systems, based on one or few experimental data might lead to a general decrease of the database quality in other compositional and temperature ranges. The agreement between indications coming from the present study and [15], suggests that a re-evaluation of some thermodynamic parameters would probably be beneficial to the database performance but a) more experimental data in complex multicomponent systems would be needed and b) this is beyond the goal of the present work, mostly focused on the differences between the two proposed synthesis routes. For the FCC phase, on the contrary, the agreement between calculated and experimental phase amounts and compositions is satisfactory.

Thermal treatments, micro-hardness measurements and average grain size of the FCC phase in the different samples are summarized in Table 8. The milling + SPS synthesis route drastically decreases the grain size of the FCC phase, which passes from several tens of microns for the AM samples to less than a micron for the SPS ones. For both preparation methods the heat treatment increases the value of $HV_{0.5}$. More comments on the effect of annealing on the hardness of the different samples can be found in Sections 4.1 and 4.2 for the AM and SPS series of samples, respectively. The SPS processed samples are systematically harder than those prepared by AM, most likely due to thinner grain and to the fine dispersion of μ crystals in the matrix, together with the significant presence of Al_2O_3 segregating at grain boundaries.

Table 7
FCC and μ phases compositions measured by EDS (mol %) for the samples showing coexistence of both phases.

		Al	Co	Cr	Fe	Ni	W
μ phase	**AM_1100**	–	18.8	20.1	15.7	9.0	36.4
	SPS_AS	0.4	17.9	20.2	15.2	5.8	40.5
	SPS_1100_FC	0.4	17.9	19.7	15.3	8.7	38.0
	CALC_GHEA_1100 °C	–	24.9	8.0	11.2	9.8	46.1
FCC	**AM_1100**	3.1	23.5	22.9	23.5	23.5	3.5
	SPS_AS	2.3	24.4	24.2	24.6	21.7	2.8
	SPS_1100_FC	2.1	24.0	23.6	23.9	23.2	3.2
	CALC_GHEA_1100 °C	3.5	23.2	23.5	23.5	23.5	2.8

Table 8
Phases, hardness, thermal treatment and average grain size of FCC in the different samples.

Sample/ Alloy	Phases	$HV_{0.5}$	Thermal Treatment	Average FCC grain size
AM	FCC	382 ± 5	as-cast	~20–40[a] μm
AM_1100	FCC + μ	233 ± 16	Annealed 14d at 1100 °C and quenched	~60–80 μm
SPS	FCC + μ	600 ± 15	Spark plasma sintered at 1100 °C	~0.4 μm
SPS_1100	FCC	300 ± 1	Spark plasma sintered at 1100 °C, annealed 14d at 1100 °C and quenched	~0.8 μm
SPS_1100_FC	FCC + μ	330 ± 3	Spark plasma sintered, annealed 14d at 1100 °C and furnace cooled	~0.8–1 μm

[a] Estimated based on previous experiences on alloys of this kind (see supplementary material S2).

5. Conclusions

In the present work, a six-component HEA of $Al_{0.15}CoCrFeNiW_{0.15}$ composition has been designed, prepared by both AM and SPS, thermally treated, and finally characterized. CALPHAD thermodynamic calculations have been used to choose the target composition and to compare with the experimental results, obtaining satisfactory agreement. The samples preparation method has a substantial effect on the final features of the alloy, such as microstructure and micro-hardness. AM produces a monophasic FCC microstructure, characterized by larger grains of some tenths of microns (estimated ~ 20–40 μm), while a very fine nanostructured FCC (~0.4 μm) + μ precipitates microstructure, characterized by the presence of Al_2O_3 particles, is obtained by SPS. No interaction between such Al_2O_3 particles and the metal HEA matrix was observed, regardless of the thermal treatment. After annealing at 1100 °C, the microstructure and phases analyses of arc melted samples reveal a closer agreement with the thermodynamic calculations. On the contrary, the small grain size (~0.4 μm) in the case of the SPS_1100 sample is responsible for the enhanced W solubility in the FCC solid solution via Gibbs-Thomson effect, which lead to the dissolution of the μ phase present in the SPS_AS sample. Annealing followed by furnace cooling, however, allows the reprecipitation of the μ phase over cooling. As for the alloy overall micro-hardness, SPS samples systematically show higher values of $HV_{0.5}$, most likely thanks to the smaller grains dimension and to the presence of finely dispersed μ phase crystals. Summarizing, this work remarks how: a) CALPHAD can be used to effectively support experimental investigations (selection of promising compositions, result interpretation, etc.) in complex multicomponent systems; b) the AM procedure can be exploited to reach homogenous and monophasic FCC HEAs; c) mechanical alloying by ball milling of elemental powders leads to FCC solid solution despite the presence of some residual W; d) the SPS procedure is successful in eliminating all traces of residual W and can be effectively employed to produce nanostructured HEAs with potentially interesting features; e) the grain size is extremely relevant in determining properties and microstructural evolution of the same composition prepared by different methods. By emphasizing the variation in final microstructural characteristics depending on the preparation method, these findings support the utilization of HEAs across diverse application areas. This includes for instance their potential use in bulk form with tailored microstructures, as well as in powder form for further processing in additive manufacturing.

CRediT authorship contribution statement

L. Fenocchio: Conceptualization, Methodology, Validation, Investigation, Data curation, Writing – original draft. **A. Saviot:** Conceptualization, Methodology, Validation, Investigation, Data curation, Writing – original draft. **S. Gambaro:** Conceptualization, Methodology, Validation, Investigation, Data curation, Writing – review & editing. **S. Le Gallet:** Conceptualization, Methodology, Validation, Writing – review & editing. **F. Valenza:** Conceptualization, Methodology, Validation, Supervision, Writing – review & editing. **M.R. Ardigo-Besnard:** Conceptualization, Methodology, Validation, Supervision, Writing – review & editing. **G. Cacciamani:** Conceptualization, Methodology, Validation, Supervision, Writing – review & editing.

Declaration of competing interest

The authors declare that they have no known competing financial interests or personal relationships that could have appeared to influence the work reported in this paper.

Acknowledgments

The authors would like to thank: Dr. Carlo Alberto Biffi and Dr. Jacopo Fiocchi from CNR-ICMATE (Lecco) for the support with one of the thermal treatments; Dr. Walter Sgroi, Dr. Annabella Covazzi and Enrico Puzo for the experimental support for the etching and SEM observation of the AM samples; Prof. Paola Riani for the suggestions and discussions about micrographs and XRD.

Appendix A. Supplementary data

Supplementary data to this article can be found online at https://doi.org/10.1016/j.jmrt.2024.12.140.

References

[1] Cantor B, Chang ITH, Knight P, Vincent AJB. Microstructural development in equiatomic multicomponent alloys. Mater Sci Eng, A Jul. 2004;375(377):213–8. https://doi.org/10.1016/j.msea.2003.10.257.
[2] Yeh J-W, et al. Nanostructured high-entropy alloys with multiple principal elements: novel alloy design concepts and outcomes. Adv Eng Mater 2004;6(5):299–303. https://doi.org/10.1002/adem.200300567.
[3] Miracle DB, Senkov ON. A critical review of high entropy alloys and related concepts. Acta Mater Jan. 2017;122:448–511. https://doi.org/10.1016/j.actamat.2016.08.081.
[4] Laurent-Brocq M, Couzinié J-P. Alliages multi-composants à haute entropie - Concepts, microstructures et propriétés mécaniques. Étude et propriétés des métaux. Jan. 2018. https://doi.org/10.51257/a-v1-re269.
[5] Tokarewicz M, Grądzka-Dahlke M. Review of recent research on AlCoCrFeNi high-entropy alloy. Metals Aug. 2021;11(8):1302. https://doi.org/10.3390/met11081302.
[6] Zhou YJ, Zhang Y, Wang YL, Chen GL. Solid solution alloys of $AlCoCrFeNiTi_x$ with excellent room-temperature mechanical properties. Appl Phys Lett Apr. 2007;90(18):181904. https://doi.org/10.1063/1.2734517.
[7] Ma SG, Zhang Y. Effect of Nb addition on the microstructure and properties of AlCoCrFeNi high-entropy alloy. Mater Sci Eng, A Jan. 2012;532:480–6. https://doi.org/10.1016/j.msea.2011.10.110.
[8] Chen J, et al. Effect of Zr content on microstructure and mechanical properties of AlCoCrFeNi high entropy alloy. Mater Des Mar. 2016;94:39–44. https://doi.org/10.1016/j.matdes.2016.01.033.
[9] Dong Y, Zhou K, Lu Y, Gao X, Wang T, Li T. Effect of vanadium addition on the microstructure and properties of AlCoCrFeNi high entropy alloy. Mater Des May 2014;57:67–72. https://doi.org/10.1016/j.matdes.2013.12.048.
[10] Fourmont A, Le Gallet S, Politano O, Desgranges C, Baras F. Effects of planetary ball milling on AlCoCrFeNi high entropy alloys prepared by Spark Plasma Sintering: experiments and molecular dynamics study. J Alloys Compd Apr. 2020;820:153448. https://doi.org/10.1016/j.jallcom.2019.153448.
[11] Zhang A, Han J, Meng J, Su B, Li P. Rapid preparation of AlCoCrFeNi high entropy alloy by spark plasma sintering from elemental powder mixture. Mater Lett Oct. 2016;181:82–5. https://doi.org/10.1016/j.matlet.2016.06.014.
[12] Couret A, et al. Chemical heterogeneities in tungsten containing TiAl alloys processed by powder metallurgy. Materialia Aug. 2021;18:101147. https://doi.org/10.1016/j.mtla.2021.101147.
[13] Saviot A, et al. Phase and microstructure formation during reactive spark plasma sintering of $Al_xCoCrFeNi$ (x=0.3 and 1) high entropy alloys. J Mater Res Technol Sep. 2024;32:3047–59. https://doi.org/10.1016/j.jmrt.2024.08.096.
[14] Ostrowska M, Riani P, Bocklund B, Liu Z-K, Cacciamani G. Thermodynamic modeling of the Al-Co-Cr-Fe-Ni high entropy alloys supported by key experiments. J Alloys Compd Mar. 2022;897:162722. https://doi.org/10.1016/j.jallcom.2021.162722.
[15] Gambaro S, Fenocchio L, Valenza F, Riani P, Cacciamani G. Combined experimental and CALPHAD investigation of equimolar AlCoCrFeNiX (X=Mo,Ta, W) high-entropy alloys. Calphad Jun. 2024;85:102702. https://doi.org/10.1016/j.calphad.2024.102702.
[16] Gambaro S, Valenza F, Fenocchio L, Cacciamani G. Liquid AlCoCrFeNi and AlCoCrFeNiX (X = Mo, Ta) high-entropy alloys on graphite: wetting, reactivity and CALPHAD modelling. Surface Interfac Oct. 2024:105207. https://doi.org/10.1016/j.surfin.2024.105207.
[17] Dasari S, et al. Recovery of cold-worked $Al_{0.3}CoCrFeNi$ complex concentrated alloy through twinning assisted B2 precipitation. Acta Mater Jan. 2021;202:448–62. https://doi.org/10.1016/j.actamat.2020.10.071.
[18] Shi ZJ, Wang ZB, Wang XD, Zhang S, Zheng YG. Effect of thermally induced B2 phase on the corrosion behavior of an $Al_{0.3}CoCrFeNi$ high entropy alloy. J Alloys Compd May 2022;903:163886. https://doi.org/10.1016/j.jallcom.2022.163886.
[19] Wang W, Zhou W, Song S, Reddy KM, Wang X. Effect of deformation induced B2 precipitates on the microstructure and mechanical property of $Al_{0.3}CoCrFeNi$ high-entropy alloy. J Alloys Compd Apr. 2020;821:153445. https://doi.org/10.1016/j.jallcom.2019.153445.
[20] Dong Y, Lu Y. Effects of tungsten addition on the microstructure and mechanical properties of near-eutectic $AlCoCrFeNi_2$ high-entropy alloy. J Mater Eng Perform Jan. 2018;27(1):109–15. https://doi.org/10.1007/s11665-017-3096-6.
[21] Ostrowska M, Cacciamani G. Thermodynamic modelling of the σ and μ phases in several ternary systems containing Co, Cr, Fe, Mo, Re and W. J Alloys Compd Dec. 2020;845:156122. https://doi.org/10.1016/j.jallcom.2020.156122.

[22] Cacciamani G, Roncallo G, Wang Y, Vacchieri E, Costa A. Thermodynamic modelling of a six component (C-Co-Cr-Ni-Ta-W) system for the simulation of Cobalt based alloys. J Alloys Compd Jan. 2018;730:291–310. https://doi.org/10.1016/j.jallcom.2017.09.327.
[23] Wang Y, Ostrowska M, Cacciamani G. Thermodynamic modeling of selected ternary systems containing Y and CALPHAD simulation of CoNiCrAlY metallic coatings. Calphad Mar. 2021;72:102214. https://doi.org/10.1016/j.calphad.2020.102214.
[24] Berthod P. Carbides and carbon control in MC – reinforced superalloys. Asian Journal of Chemical Sciences Dec. 2020:64–74. https://doi.org/10.9734/ajocs/2020/v8i419056.
[25] Cartón-Cordero M, et al. Microstructure and compression strength of Co-based superalloys hardened by γ′ and carbide precipitation. Mater Sci Eng, A Sep. 2018;734:437–44. https://doi.org/10.1016/j.msea.2018.08.007.
[26] Bae JW, Park JM, Moon J, Choi WM, Lee B-J, Kim HS. Effect of μ-precipitates on the microstructure and mechanical properties of non-equiatomic CoCrFeNiMo medium-entropy alloys. J Alloys Compd Apr. 2019;781:75–83. https://doi.org/10.1016/j.jallcom.2018.12.040.
[27] Aizenshtein M, Strumza E, Brosh E, Hayun S. Precipitation kinetics, microstructure, and equilibrium state of A2 and B2 phases in multicomponent $Al_{2.75}$CoCrFeNi alloy. J Mater Sci Jun. 2020;55(16):7016–28. https://doi.org/10.1007/s10853-020-04487-9.
[28] Beltrame C. "Studio di High Entropy Alloys (HEA) per applicazioni ad alta temperatura" (in Italian) -. In: "High entropy alloys' (HEA) study for high temperature applications", bachelor thesis. Università di Genova; Feb. 2024. Available at: https://unire.unige.it/handle/123456789/7745.
[29] Ren H, et al. High-performance AlCoCrFeNi high entropy alloy with marine application perspective. J Mater Res Technol Jul. 2023;25:6751–63. https://doi.org/10.1016/j.jmrt.2023.07.135.
[30] Humphreys J, Rohrer GS, Rollett A. Chapter 7 - recrystallization of single-phase alloys. In: Humphreys J, Rohrer GS, Rollett A, editors. Recrystallization and related annealing phenomena. third ed. Oxford: Elsevier; 2017. p. 245–304. https://doi.org/10.1016/B978-0-08-098235-9.00007-0.
[31] Liu X-F, et al. Self-sharpening' tungsten high-entropy alloy. Acta Mater Mar. 2020;186:257–66. https://doi.org/10.1016/j.actamat.2020.01.005.
[32] Liu T-W, Li T, Dai L-H. Near-equiatomic μ phase in self-sharpening tungsten-based high-entropy alloys. Metals Jul. 2022;12(7). https://doi.org/10.3390/met12071130. Art. no. 7.
[33] Suryanarayana C. Mechanical alloying and milling. Prog Mater Sci Jan. 2001;46(1):1–184. https://doi.org/10.1016/S0079-6425(99)00010-9.
[34] Guillon O, et al. Field-Assisted sintering technology/spark plasma sintering: mechanisms, materials, and technology developments. Adv Eng Mater 2014;16(7):830–49. https://doi.org/10.1002/adem.201300409.
[35] John R, et al. Influence of mechanically activated annealing on phase evolution in $Al_{0.3}$CoCrFeNi high-entropy alloy. J Mater Sci Dec. 2019;54(23):14588–98. https://doi.org/10.1007/s10853-019-03917-7.
[36] Ida S, Yamagata R, Nakashima H, Kobayashi S, Takeyama M. Grain boundary precipitation control of GCP phase using TCP or A2 phase in Ni-based alloys. Metals Nov. 2022;12(11). https://doi.org/10.3390/met12111817. Art. no. 11.
[37] Ida S, Kobayashi S, Takeyama M. Grain boundary precipitation behavior of δ-Ni_3Nb (D0a) phase in a Ni-Nb-Fe ternary model alloy. J Alloys Compd Oct. 2018;764:1033–8. https://doi.org/10.1016/j.jallcom.2018.05.169.
[38] Perez M. Gibbs–Thomson effects in phase transformations. Scripta Mater Apr. 2005;52(8):709–12. https://doi.org/10.1016/j.scriptamat.2004.12.026.
[39] Moszyński D, Moszyńska I, Arabczyk W. The transformation of α–Fe into γ′–Fe4N in nanocrystalline Fe–N system: influence of Gibbs–Thomson effect. Appl Phys Lett Dec. 2013;103(25):253108. https://doi.org/10.1063/1.4851155.